Mercury's magnetosphere-solar wind interaction for northward and southward interplanetary magnetic field: Hybrid simulation results

Pavel M. Trávníček[a,b,c], David Schriver[a], Petr Hellinger[b,c], David Herčík[c], Brian J. Anderson[d], Menelaos Sarantos[e], James A. Slavin[e]

[a]*Institute of Geophysics and Planetary Physics, University of California, Los Angeles, CA, 90095-1567, U.S.A.*
[b]*Astronomical Institute, Academy of Sciences of the Czech Republic, Bocni II/1401, 14131 Prague, Czech Republic*
[c]*Institute of Atmospheric Physics, Academy of Sciences of the Czech Republic, Bocni II/1401, 14131 Prague, Czech Republic*
[d]*Johns Hopkins University Applied Physics Laboratory, Laurel, MD, 20723, U.S.A.*
[e]*Heliophysics Science Division, NASA Goddard Space Flight Center, Greenbelt, MD, 20771, U.S.A.*

Abstract

Analysis of global hybrid simulations of Mercury's magnetosphere-solar wind interaction is presented for northward and southward Interplanetary Magnetic Field (IMF) orientations in the context of MESSENGER's first two encounters with Mercury. The global kinetic simulations reveal the basic structure of this interaction, including a bow shock, ion foreshock, magnetosheath, cusp regions, magnetopause, and a closed ion ring belt formed around the planet within the magnetosphere. The two different IMF orientations induce different locations of ion foreshock and different magnetospheric properties: the dayside magnetosphere is smaller and cusps are at lower latitudes for southward IMF compared to northward IMF whereas for southward IMF the nightside magnetosphere is larger and exhibits a thin current sheet with signatures of magnetic reconnection and plasmoid formation. For the two IMF orientations the ion foreshock and quasi-parallel magnetosheath manifest ion-beam-driven large-amplitude oscillations whereas the quasi-perpendicular magnetosheath shows ion-temperature-anisotropy driven wave activity. The ions in Mercury's belt remain quasi-trapped for a limited time before they are either absorbed by Mercury's surface or escape from the magnetosphere. The simulation results are compared with MESSENGER's observations.

Preprint submitted to Icarus *November 24, 2009*

Key words: Mercury, magnetospheres, solar wind

1. Introduction

The MErcury Surface, Space ENvironment, GEochemistry, and Ranging (MESSENGER) spacecraft was launched in 2004 to address a number of outstanding scientific questions related to Mercury, including the chemical composition of the planetary surface, the planet's geological history, the size and state of the core, the nature of Mercury's magnetic field, the volatile inventory at the poles, and the nature of Mercury's exosphere and magnetosphere (Solomon et al., 2001). The orbital phase of the mission will not begin until 2011, but thus far the satellite has made two flybys of Mercury, the first on 14 January 2008, and the second on 6 October 2008 (a third flyby will occur on 29 September 2009).

Observations by the Mariner 10 flybys in the 1970s and the recent MESSENGER flybys have firmly established that Mercury has an intrinsic magnetic field that is dominantly dipolar in geometry. On the basis of both the MESSENGER data and earlier Mariner 10 data, the dipole moment is estimated to be about 250 nT R_M^3, where R_M is the radius of Mercury (2439 km), with no more than a 5° dipole tilt with respect to the rotation axis and with the magnetic moment pointing below the ecliptic plane, i.e., in the same sense as Earth (Ness et al., 1974, 1975, 1976; Jackson and Beard, 1977; Whang, 1977; Anderson et al., 2008). As such, the solar wind interaction with the intrinsic magnetic field of Mercury results in a magnetosphere with many features similar to Earth's magnetosphere, i.e., a bow shock, magnetosheath, magnetopause, cusps, and a magnetotail (Russell et al., 1988; Slavin et al., 2007; Fujimoto et al., 2007; Slavin et al., 2008, 2009). Compared with that of Earth, however, Mercury's magnetosphere is much smaller because of its weaker magnetic dipole moment, and the estimated standoff distance between the planetary intrinsic magnetic field and the solar wind (magnetopause dayside nose location) for typical solar wind conditions is about 1.3–2.1 R_M (Siscoe and Christopher, 1975; Ness et al., 1976; Slavin and Holzer, 1979; Russell et al., 1988; Slavin et al., 2008). For comparison, at Earth the typical quiet-time magnetopause nose location is about 10-11 R_E ($R_E = 6371$ km).

The trajectories of the MESSENGER spacecraft during the two flybys were very similar: the satellite was nearly in the equatorial plane (see Fig. 1), within about 0.1 R_M for the entire path, and approached Mercury from the nightside-dusk sector, crossed the bow shock and magnetopause on the anti-sunward side of the planet, crossed into the nightside magnetotail, passed through closest approach

(about 200 km from the planet's surface) in the post-midnight sector, and then on the outbound leg crossed the magnetopause and reentered the solar wind in the morning-dayside sector (Solomon et al., 2008; Slavin et al., 2008, 2009). Because of pointing constraints on MESSENGER's sunshade, direct plasma measurements of the solar wind data could not be acquired, and quantities such as solar wind velocity and density have be inferred from global solar wind models (Baker et al., 2009), and from the measured location of Mercury's magnetopause during the MESSENGER flybys (e.g., Slavin et al., 2009). The Sun was in a relatively quiet state for much of 2008, and during the flybys there were no solar disturbances. The solar wind was relatively steady with an inferred speed of 400–450 km s^{-1} and dynamic pressure of about 20 pPa (Baker et al., 2009).

The onboard Magnetometer (MAG), however, was able to measure the solar wind interplanetary magnetic field (IMF) just before MESSENGER entered Mercury's magnetosphere and after exiting the magnetosphere back into the upstream solar wind. The IMF was almost ideally aligned for the two MESSENGER flybys to carry out a magnetospheric case study in the sense that for the first flyby on 14 January 2008, referred to hereafter as M1, the IMF was primarily aligned northward (Anderson et al., 2008; Slavin et al., 2008), whereas for the second flyby on 6 October 2008, referred to hereafter as M2, was primarily southward (Anderson et al., 2009; Slavin et al., 2009). For both M1 and M2 the IMF also had a large radial component (planetward magnetic field). Thus for the most part the solar wind conditions were nearly the same for M1 and M2, except for the IMF orientation. The IMF orientation is very important in determining where magnetic reconnection between the solar wind and the planetary magnetic field occurs. Magnetic reconnection results in energy conversion, allowing an exchange of flux between solar wind and magnetospheric plasmas to occur, and is a major factor in the structure and dynamics of planetary magnetospheres (Dungey, 1961; Sonnerup et al., 1981; Cowley, 1982). When the IMF is northward, as occurred during M1, reconnection between the solar wind and the magnetosphere can occur at high latitudes but is less efficient in transferring energy into the magnetosphere, whereas when the IMF is southward, as during M2, reconnection occurs near the dayside nose of the magnetopause, resulting in a more efficient transfer of energy and flux into the magnetosphere, and ultimately drives reconnection, strong planetward convection (Dungey, 1961), and geomagnetic activity in the nightside magnetotail (e.g., Baker et al., 1996). It is uncertain whether there are geomagnetic substorms at Mercury similar those observed at Earth (e.g., Russell and McPherron, 1973), but strong magnetic activity and energetic particle bursts indicative of substorm-like events were observed by Mariner 10 (Siscoe et al., 1975; Eraker and Simpson,

1986), and magnetic flux ropes, plasmoids, and a more dynamic magnetospheric state was detected during southward IMF during M2 (Slavin et al., 2009).

Most of the previous simulations of Mercury's magnetosphere interaction with the solar wind were done within the MHD framework (e.g., Ip and Kopp, 2002; Kabin et al., 2008). These simulations provide an overall structure of the interaction in agreement with the observations on global scales but do not include kinetic scales. To support the MESSENGER flyby data and put the results in a global context including ion kinetic effects, 3-D hybrid simulations have been carried out to model the interaction of the solar wind with a planetary magnetic field having a dipole moment similar to that of Mercury. Hybrid codes self-consistently describe the dynamics of collisionless plasmas with ions treated as kinetic particles and isothermal electrons considered as a massless fluid (e.g., Winske, 1985; Matthews, 1994; Lipatov, 2002). The hybrid code utilized in this paper has been used previously to examine the general structure of Mercury's magnetosphere for high and low solar wind pressures and showed, for example, the existence of an upstream foreshock, a magnetotail with reconnection occurring about 2.5 R_M downtail, and a belt of quasi-trapped ions that formed around the planet (Trávníček et al., 2007a, 2009).

In this paper, hybrid simulation results for runs with similar solar wind conditions to those encountered during M1 and M2 will be compared with the MESSENGER data along its trajectories during the two flybys. The differences between the two cases will be discussed in terms of overall magnetospheric structure, with the focus on the importance of ion kinetic effects, i.e., velocity distribution functions, wave generation, and wave-particle interactions. The qualitative state of Mercury's magnetosphere during the flybys as deduced from MESSENGER data is summarized in Fig. 1 Slavin et al. (2008, 2009).

The paper is structured as follows. In section 2, the hybrid simulation model of Mercury is described. In section 3, a summary of MESSENGER particle and magnetic field data during virtual flybys in the simulated data is presented. In section 4, the model limitations are discussed. The paper concludes in section 5 with an overall assessment of the comparison between model and data and implications for aspects of the kinetics of Mercury's magnetosphere and of magnetospheres in general.

2. Hybrid Simulation Model

An earlier simulation study of Mercury's magnetosphere that used the same hybrid code as that employed here (Trávníček et al., 2009) focused on a qualita-

tive comparison between the 3-D global hybrid simulation and MESSENGER observations acquired during the spacecraft's first Mercury's flyby. Trávníček et al. (2009) assumed that the solar wind IMF was oriented in the equatorial plane, i.e., $B_z = 0$. Here we investigate the influence of northward ($B_z > 0$) and southward ($B_z < 0$) IMF orientation on the interaction of Mercury's magnetosphere with the solar wind.

As in the previous simulation (Trávníček et al., 2009), we here use a scaled down model of Mercury with a magnetic moment $M = 50,000 B_{\rm sw} d_{p{\rm sw}}^3 4\pi/\mu_0$, (first introduced in Trávníček et al., 2007a), where $B_{\rm sw}$ is the magnitude of the solar wind magnetic field, $d_{p{\rm sw}} = c/\omega_{pp{\rm sw}}$ is the proton inertial length in the solar wind, c is the speed of light, $\omega_{pp{\rm sw}}$ is the solar wind proton plasma frequency, and μ_0 is the magnetic permeability in free space. The downscaling preserves the stand-off magnetopause distance $R_{\rm mp}$ predicted from the pressure balance between the solar wind ram pressure $P_{\rm ram,sw}$ and the magnetospheric pressure: $R_{\rm mp} = [B_{\rm eq}^2/(2\mu_0 P_{\rm ram,sw})]^{1/6} R_M$, where $B_{\rm eq}$ is the magnetic field at the equator of the planet. Although the model is scaled down, the scaled down radius R_M always remains much larger than the local proton Larmor radius.

For the simulations here we use a 3-D simulation box with $657 \times 288 \times 288$ mesh points distributed equidistantly along the three (Cartesian) dimensions with the spatial resolution $\Delta x = 0.4\, d_{p{\rm sw}}$, $\Delta y = \Delta z = d_{p{\rm sw}}$, i.e., the size of the simulation domain is $237.6 \times 288 \times 288\, d_{p{\rm sw}}^3$. Macro-particles are advanced with the time step $\Delta t = 0.02\, \omega_{gp{\rm sw}}^{-1}$, where $\omega_{gp{\rm sw}}$ is the solar wind proton gyrofrequency; whereas the electromagnetic fields are advanced with the finer time resolution $\Delta t_B = \Delta t/20$.

The magnetic field is initialized with a superposition of the homogeneous IMF $\boldsymbol{B}_{\rm sw}$ and a dipolar planetary magnetic field $\boldsymbol{B}_M$. The IMF $\boldsymbol{B}_{\rm sw} = (B_x, 0, B_z)$, $B_{\rm sw} = 1$, makes an angle $\varphi = \pm 20^\circ$ with respect to the $+X$ axis (i.e., with respect to the solar-wind flow direction) in the plane (X, Z) of the main Mercury meridian. Here we refer to the simulation with northward IMF ($\varphi = 20^\circ$) as to Hyb1 and to the simulation with southward IMF ($\varphi = -20^\circ$) as to Hyb2. The dipolar field is defined by

$$\boldsymbol{B}_M = \frac{\mu_0}{4\pi} \frac{M}{r^3} \left(-2\, \sin\lambda\, \boldsymbol{e}_r + \cos\lambda\, \boldsymbol{e}_\lambda\right), \tag{1}$$

where the magnetic moment M is Mercury's magnetic moment and r is the radial distance from the center of Mercury, $\boldsymbol{e}_r$ and $\boldsymbol{e}_\lambda$ are unit vectors in the radial and magnetic latitude directions, respectively, and λ is the magnetic latitude measured from the equatorial plane (X, Y) (no tilt of the planetary dipole is applied). The

superposition approach provides a simple way to initialize the simulation box with a divergence-free magnetic field throughout the simulation box. We assume that the superimposed IMF represents a negligible perturbation to the modeled planetary magnetic field and, similarly, the superimposed dipolar field ($B_M \propto 1/r^3$, Eq. 1) contributes negligibly to the IMF (Trávníček et al., 2007a, 2009). For both the simulations we also use a flat resistivity $\eta = 0.1\mu_0 v_{A\mathrm{sw}}^2/\omega_{gp\mathrm{sw}}$ in the entire simulation box, where $v_{A\mathrm{sw}}$ is the Alfvén velocity in the solar wind.

At $t = 0$ the simulation box is loaded with 80 and 50 macro-particles in each cell outside the planet for simulation Hyb1 and Hyb2, respectively, representing the solar wind Maxwellian isotropic protons with the density $n_p = n_{p\mathrm{sw}}$ and the bulk speed $\boldsymbol{v}_p = (4v_{A\mathrm{sw}}, 0, 0)$. This plasma flow is continuously injected from the left boundary of the simulation box at $X = -5.15\,R_M$. The ratio of proton (electron) to magnetic pressure in the solar wind is $\beta_{p\mathrm{sw}} = \beta_{e\mathrm{sw}} = 1$. An overview of the simulation parameters is given in Table 1.

We use open boundary conditions, i.e., macro-particles freely leave the simulation box on all sides. Macro-particles hitting the planetary surface (set at $R_M = 15.32\,d_{p\mathrm{sw}}$) are removed from the simulation. We keep $\partial\boldsymbol{B}/\partial t = 0$ in the interior of the planet and $\partial\boldsymbol{E}/\partial r = 0$. An additional resistivity layer $\eta \approx 0.8\exp\left(-h^2/h_0^2\right)$, where h is radial distance from the surface and $h_0 = 3\,d_{p\mathrm{sw}}$, is applied near the planet's surface. We have also injected H^+ ions with density of order $n_p \sim 10^{-4}\,n_{p\mathrm{sw}}$ isotropically from Mercury's surface with velocity $v_p \sim 0.05\,v_{A\mathrm{sw}}$ normal to the surface. Both numerical experiments Hyb1 and Hyb2 reached the time $120\,\omega_{gp\mathrm{sw}}^{-1}$, which is sufficiently long compared with the system transit time and which allowed a formation of a quasi-stationary magnetosphere-solar wind interaction in both cases.

3. Simulation Results

3.1. Global structure

We examine the differences between the response of Mercury's magnetosphere to the solar wind with the IMF defined within the plane of Mercury's noon-midnight meridian (X, Z) oriented northward (numerical experiment Hyb1) and southward IMF orientation (numerical experiment Hyb2) using the hybrid simulation model described in the previous section. Our goal is not to perform an exact two-case study for the M1 and M2 events, but rather to seek conditions requiring modification to the least number of simulation parameters that permit the simulation to be compared with the MESSENGER data, as well as comparing the two simulations with one another.

A comparison between the two global kinetic models is displayed in Fig. 2 shows the color-scale plots of the proton density $n_p/n_{p\mathrm{sw}}$ in the equatorial plane (X, Y) and in the plane of the noon-midnight meridian (X, Z) from the two simulation Hyb1 (panels a and b) and Hyb2 (panels c and d). White dashed lines denote projections of the corresponding trajectories of the MESSENGER spacecraft on 14 January 2008 (M1) and on 6 October 2008 (M2) onto the corresponding plane. Colored bullets demarcate various boundaries along the trajectories for better orientation and their overview of the markers is given in Table 2.

Figure 2 shows that the plasma is being compressed behind the shock and in the dayside magnetosheath and expands further downstream. The magnetosheath is connected to well-pronounced cusps. The plasma density is depleted in the magnetosphere/magnetotail regions. Figure 2 demonstrates that the different IMF orientations lead to changes in several macroscopic features of Mercury's magnetosphere. For example, the proton foreshock that results from the proton reflection off the quasi-parallel bow shock (and/or from the leakage from downstream) forms to the south and north of the equatorial plane when the IMF is northward and southward, respectively (e.g., Fig. 2bd). Moreover the M2 trajectory at its outbound bow-shock crossing enters the proton foreshock more deeply compared to the case of trajectory M1 in simulation Hyb1. Also, the plasma sheet and the current sheet are much thinner (with a thickness comparable to the proton gyroradius just outside the sheet) for southward IMF than for northward IMF, and as such they efficiently support formation of reconnection points and plasmoids. A preliminary study of the magnetotail evolution under southward IMF indicates repeated reconnection and plasmoid formation (see Fig. 3). A more quantitative examination of these phenomena is beyond the scope of this study.

Cusps form on the dayside, and the angle between northern and southern cusp locations is smaller (and the dayside magnetosphere is smaller as expected, cf., Slavin and Holzer, 1979) in the case of southward IMF. This is likely because of the different reconnection regions for the two IMF orientations. The cusp protons have an averaged velocity directed planetward and this flow is flow is stronger in the case of northward IMF which is compatible with high latitude reconnection (Lavraud et al., 2005). Another macroscopic feature that changes with the IMF conditions is the size of the magnetospheric cavity in the Z direction (see Fig. 2bd).

Figure 3 shows an example of a plasmoid formed in the magnetotail marked by a white arrow on Fig. 3a in the case with southward IMF. The pasmoid is identified in panel 3c by the bi-polar signature in the Z-component of the magnetic field B_z. It can also be seen that within the plasmoid the density n_p peaks (see

Fig. 3b) and the total magnetic field minimizes (see Fig. 3d). The plasmoid structure has roughly $0.5\,R_M$ in diameter (see Fig. 3bcd) and its life-span from time of its formation to its dissipation is $\approx 10 - 20\,\omega_{gp\mathrm{sw}}^{-1}$. The plasmoid tends to move slowly down the magnetotail away from the planet.

For further investigation of these global features we look next at the curved sectional planes of the 3-D simulation box, which contain the spacecraft trajectory (M1 or M2) and are perpendicular to the equatorial plane (X, Y). Figure 4 shows color-scale plots of the simulated proton density $n_p/n_{p\mathrm{sw}}$ in the two-dimensional sectional curved planes as a function of r and Z, where r is the distance of the corresponding position of the spacecraft from Mercury's surface. The dashed white lines corresponds to the trajectories M1 and M2 of the spacecraft. The upper panel (a) shows the case with northward IMF (Hyb1/M1) and the lower panel (b) shows the case with southward IMF (Hyb2/M2). Colored vertical bars on the panels correspond to the colored bullets used as orientation markers along the spacecraft trajectory on Fig. 2 (see also Table 2). The results show the same differences in macroscopic features of Mercury's magnetosphere between the two studied cases of northward and southward IMF as was observed on Fig. 2. The proton foreshock is below and above the equatorial plane in the case of northward and southward IMF, respectively. The M2 trajectory on its outbound bow-shock crossing enters the proton foreshock more strongly than for M1. The plasma sheet and current sheet for the southward IMF are clearly much thinner. The magnetospheric cavity is wider in the Z direction in the case of southward IMF compared to northward IMF (and consequently, the bow shock is slightly wider in that case). This may be partly explained by fact that the plasma within the magnetosphere provides higher pressure on the magnetopause from inside in the case of southward IMF; we shall return to this question later. In both cases a plasma density depletion can be seen near the point of closest approach "CA" surrounded by the quasi-trapped belt ions as the probe flies very close to Mercury's surface below Mercury's plasma belt.

The magnitude of the simulated magnetic field B/B_{sw} in the same curved sectional planes of Fig. 4 which contain the spacecraft trajectory (M1 or M2) and are perpendicular to the equatorial plane (X, Y) is shown as a gray-scale plot in Fig. 5. Upper panel (a) shows the simulated magnetic field B/B_{sw} from the simulation Hyb1 (northward IMF) at simulation time $t = 100\,\omega_{gp\mathrm{sw}}^{-1}$ with the scaled trajectory of the MESSENGER spacecraft from 14 January 2008. Bottom panel (b) shows the simulated magnetic field B/B_{sw} from the simulation Hyb2 (southward IMF) at simulation time $t = 100\,\omega_{gp\mathrm{sw}}^{-1}$ with the scaled and projected trajectory of the MESSENGER spacecraft from 6 October 2008. The magnetic structure of the current sheet is more complex during northward IMF (Fig. 5a)

when the current sheet is thicker (see also Figs. 2b and 4a). Figure 5 also shows diamagnetic decreases in the magnetosphere in the vicinity of the equatorial plane due to the presence of belt particles (compare Figs. 5 and 4).

The magnetopause (regions of $B \approx 0$) is pronounced in the northern and southern hemispheres in the case of northward IMF. In the case of the southward IMF (Fig. 5b), the current sheet is much thiner and its location is well defined and less structured (see also Figs. 2d and 4b). However, the magnetopause does not contain clear regions with $B \approx 0$. Note that the spacecraft clearly passes through upstream outbound bow-shock foot oscillations in the case of southward IMF as it flies through the proton foreshock.

3.2. Data along spacecraft trajectories

For a better comparison between the simulation results and MESSENGER observations we next concentrate on the simulated data along the trajectories corresponding to the two MESSENGER flybys. For the two runs Hyb1 and Hyb2 the virtual data were acquired along the M1 and M2 trajectories, respectively. There are over 8000 virtual measurements with two consecutive measurement points separated by $\Delta r \sim 0.1 d_{p\mathrm{sw}}$ Note that the spatial sampling of the trajectory of the virtual spacecraft is slightly better than the spatial resolution used in the simulations ($\Delta r < \Delta x$, Δy, and Δz).

Different observables along trajectory M1 from simulation Hyb1 (northward IMF) and the same observables along trajectory M2 from simulation Hyb2 (southward IMF) are compared in Fig. 6. Panels a and g show the density $n_p/n_{p\mathrm{sw}}$, panels b and h show magnitude of the magnetic field B/B_{sw}, panels c and i display the proton plasma temperature $T_p/T_{p\mathrm{sw}} = (2T_{p\perp} + T_{p\parallel})/3/T_{p\mathrm{sw}}$, panels d and j show the proton temperature anisotropy $T_{p\perp}/T_{p\parallel}$, panels e and k show the X-component of the plasma bulk velocity $v_{px}/v_{Ap\mathrm{sw}}$, and panels f and l displays the proton kinetic pressure $p_p/p_{p\mathrm{sw}}$. Gray dashed horizontal line on panels j and k marks the value 1 and 0 of the corresponding observable, respectively. The four top panels a, g, b and h give profiles of the density and magnetic field depicted in Figs. 4 and 5. Figure 4 clearly shows the different transition regions and quantifies the previous results. For both the orientations the transition between the outbound magnetosheath and the magnetosphere happens in two places. The density and proton pressures decrease near marker "4" whereas the magnetic signatures of the magnetopause is closer to planet, marker "MO"; here the magnitude of the magnetic field increases for northward IMF and goes to the local minimum for southward IMF as well as the bulk velocity strongly decreases. Another interesting feature is the strong backstreaming ($v_{xp} < 0$) of magnetospheric plasma

(Fig. 6ek) between points "2" and "3". The spacecraft has not yet entered Mercury's plasma belt at these points in the trajectories, so the backstreaming occurs for plasma within the magnetosphere close to the magnetopause. Moreover, the same phenomenon can be seen between "CA" and "MO", but only for southward IMF. The streaming may represent plasma convected and/or accelerated planetward of the reconnection region in the magnetotail. It is much stronger in the case of southward IMF. The simulation results in the southward IMF case clearly exhibit periodic formation of plasmoids in the magnetotail (see Figure 3). This result suggests, that the dynamic pressure of magnetospheric plasma can play an important role in the positioning of the magnetopause at Mercury. The current-sheet plasma with $v_{xp} < 0$ observed between locations "2" and "3" has higher temperature (Fig. 6ci) in both cases. Protons in the magnetosheath and magnetosphere have generally higher proton temperatures perpendicular to the magnetic field ($T_{p\perp}$) than parallel to the field ($T_{p\|}$). However, the temperature anisotropy $T_{p\perp}/T_{p\|}$ drops significantly in vicinity of the current sheet, even to $T_{p\|} > T_{p\perp}$ (Fig. 6j). This behavior leads us to look at the velocity distribution functions.

The proton velocity distribution functions (VDFs) f_p along the M1 and M2 trajectories of the virtual spacecraft calculated for all macro-particles within a sphere with radius $r_{\rm vdf} = 0.9 d_{p\rm sw}$, are shown in Fig. 7. Panels show different cuts of the function f_p: (a and d) $f_x = f_p(r, v_x, 0, 0)$ (b and e) $f_y = f_p(r, 0, v_y, 0)$ and (c and f) $f_z = f_p(r, 0, 0, v_z)$. First, note the difference at the outbound bow-shock crossing at panels a and d beyond the bar "SO", when in the case of southward IMF the spacecraft enters the proton foreshock with a beam of upstream flowing plasma. Figure 7 also clearly shows the two transitions markers "MO" and "4" between the outbound magnetosheath and the magnetosphere. Note also the VDF close to white marker "2" for southward IMF (Figs. 4d, 4e, and 4f). The current sheet in this case is much thinner [see the density $n_p/n_{p\rm sw}$ in the plane (X, Z) on Fig. 4]. The spacecraft here leaves the current sheet plasma entering the magnetospheric cavity. The spacecraft is flying through the current sheet in the region between white bars "2" and "3" (compare panels a and d). In this location we observe sunward plasma streaming with $v_{px} < 0$. When the IMF is oriented southward (d), the negative velocity $v_{px} \approx -2 v_{A\rm sw}$ is more pronounced, and we observe a clear dense beam separated from the core protons likely originating from reconnection regions in the magnetotail. The fact that the plasma is composed of a proton core and beam naturally leads to larger (effective) $T_{p\|}$, which explains the drop in $T_{p\perp}/T_{p\|}$ (Fig. 6j, between white markers "2" and "3").

In both cases the spacecraft flies between the plasma belt and the surface of the planet. See the depleted proton VDFs close to the point of closest approach

marked by the red "CA" bar. The plasma in Mercury's plasma belt in general exhibits large temperature anisotropies $T_{p\perp} > T_{p\parallel}$, as the proton VDFs in Mercury's plasma belt have a large loss cone since the proton mirror points on magnetic field lines are typicaly below Mercury's surface and many of the particles are absorbed by the surface.

The precipitation of solar wind protons onto the surface of Mercury as seen in our simulations is shown in Fig. 8. Macro-particles hitting the modeled surface of Mercury were collected over a time period of $\Delta T = \omega_{gp\mathrm{sw}}^{-1}$ at $t = 100\omega_{gp\mathrm{sw}}^{-1}$. One might expect the depletion of the plasma belt within perhaps two proton Larmor radii of Mercury's surface, on the grounds that gyrating particles here do not have enough space to complete the full gyro-orbit before being absorbed by Mercury's surface. This process should lead to the precipitation of protons onto Mercury's surface at lower latitudes. However, both precipitation maps of Fig. 8 suggest, instead, that ions are absorbed by Mercury's surface mainly at high latitudes.

The simulated proton VDFs are typically far from Maxwellian with a free energy in temperature anisotropy/beam/loss cone. To assess the linear stability of the simulated plasma from linearized Vlasov-Maxwell equations, one has to take into account the full particle VDFs (e.g., beam plus core). This is largely beyond the scope of the present paper. Here we estimate the stability of plasma with respect to the four proton temperature-anisotropy-driven instabilities (Hellinger et al., 2006) assuming that the protons have bi-Maxwellian VDFs and the plasma and the ambient magnetic field are homogenous. In order to make the linear estimates comprehensive we define a distance from marginal stability (Gary et al., 1994) of the given instability (cf., Hellinger and Trávníček, 2008) in the following way:

$$\Gamma = \mathrm{sgn}(a) \left(\frac{a}{(\beta_{\parallel p} - \beta_0)^b} - \frac{T_{\perp p}}{T_{\parallel p}} + 1 \right) \tag{2}$$

where a, b, and β_0 are fitting parameters for each instability given in Table 3 (obtained by Hellinger et al., 2006); these parameters correspond to weakly unstable plasma with a maximum growth rate equal to $10^{-3}\omega_{gp}$. By the definition given in Eq. 2 positive values of Γ indicate stability with respect to the given wavw mode, whereas negative values indicate instability; a marginal stability is for Γ near zero. Figure 9 displays the distance of plasma state at given location from marginal stability Γ given by Eq. 2, along spacecraft trajectory M1 in simulation Hyb1 (left panels) and along the trajectory M2 in simulation Hyb2 (right panels) for (a and e) the proton cyclotron instability, (b and f) the mirror instability, (c and g) the parallel fire hose and (d and h) the oblique fire hose.

The overall behavior the plasma state distances from marginal stability is similar in both simulations Hyb1/M1 and Hyb2/M2. The unperturbed solar wind is stable with respect to all instabilities. For northward IMF, the inbound magnetosheath just behind the shock (panel a) is unstable with respect to the proton cyclotron instability and somewhat less unstable to the mirror instability (panel b). Further inside the magnetosheath the plasma becomes (marginally) stable with respect to the two instabilities (cf., Hellinger and Trávníček, 2005; Trávníček et al., 2007b). For southward IMF, the inbound magnetosheath is marginally stable with respect the the proton cyclotron instability, whereas the mirror instability is stable. The magnetosphere adjacent to the inbound and outbound magnetosheath is marginaly stable with respect to the proton cyclotron and mirror instabilities for both the cases. Further inside the magnetosphere is close to stable with respect to the proton cyclotron and mirror instabilities. In the vicinity of closest approach "CA" the plasma density is strongly depleted and the determination of temperatures as well as the linear predictions are problematic. The plasma is typically stable almost everywhere with respect to the fire hose instabilities, except in the outbound magnetosheath and foreshock; here, however, the proton VDFs deviate from bi-Maxwellian and the linear analysis has to be refined. For example, the clear escaping proton beam in the foreshock may drive many additional instabilities (Gary, 1991). Finally, it is important to note that the presence of strong wave activity may significantly alter the linear predictions.

Previous analyses revealed many different sources of free energy for kinetic instabilities supported by predictions based on linear Vlasov-Maxwell theory. We shall now search for corresponding wave activity. Figure 10 displays the magnetic field acquired along the M1 and M2 trajectories. First six panels show the three time-averaged magnetic components $\langle B_x \rangle$ (a/h, red line), $\langle B_y \rangle$ (b/i, green line), and $\langle B_z \rangle$ (c/j, blue line). The magnetic field components are given in units of $B_{\rm sw}$ and $\langle\rangle$ denotes a time average over 256 time steps. The second six panels display relative variations of the three magnetic components from the averaged value at time $t = 100\,\omega_{gp\rm sw}^{-1}$ $\delta B_x/\langle B \rangle = (B_x - \langle B_x \rangle)/\langle B \rangle$ (d/k, red line), $\delta B_y/\langle B \rangle = (B_y - \langle B_y \rangle)/\langle B \rangle$ (e/l, green line), and $\delta B_z/\langle B \rangle = (B_z - \langle B_z \rangle)/\langle B \rangle$ (f/m, blue line), where $\langle B \rangle = (\langle B_x \rangle^2 + \langle B_y \rangle^2 + \langle B_z \rangle^2)^{1/2}$. The last two panels (g/n) show the relative fluctuating magnetic energy $\delta B^2/\langle B \rangle^2$. The change in IMF naturally changes the orientation of magnetic field in the magnetosheath. The best example is the outbound magnetosheath between the green "MO" and yellow "SO" markers on Fig. 10c with $B_z > 0$ and $B_z < 0$ for the cases with northward and southward IMF, respectively. There is also a change in the orientation of the B_x and B_y components in the magnetosphere close to the inbound magnetopause

beyond the green bar "MI" and through the white marker "2": $B_x < 0$, $B_y > 0$ and $B_x > 0$, $B_y < 0$ for the cases with northward IMF and southward IMF respectively. The inbound magnetosheath (between the yellow "SI" and green "MI" markers) is filled by electromagnetic field oscillations in agreement with the linear predictions (Fig. 9ae), and these oscillations have larger amplitudes in the case when the IMF is northward. These results also suggest, that there are large-amplitude oscillations between marker "2" and "3" (Fig. 10k–m) as the spacecraft enters the denser current sheet. Note, however, the relative amplitude of $\delta B/\langle B\rangle$ here is enhanced since $\langle B\rangle \approx 0$. There are also clear magnetic field oscillations from the outbound magnetopause (green marker "MO") through the outbound shock (yellow marker "SO") to the foreshock in the case of southward IMF (Fig. 10k–n) and weaker oscillations in the vicinity of the outbound shock crossing in the case of northward IMF (Fig. 10d–g). In these regions linear analysis (Fig. 9cd ang gh) predicts fire hose instabilities to be (marginally) unstable, although a beam-type instability is also expected.

Temporal evolution of the absolute value of the electric field $E(r,t)/(B_{\rm sw}v_{A\rm sw})$ and magnetic field $B(r,t)/B_{\rm sw}$ along the M1 and M2 spacecraft trajectories from the simulations Hyb1 and Hyb2 are shown in Fig. 11. The spacecraft trajectory is parameterized by the distance r from Mercury's surface (horizontal axis) and time advances on these plots in the vertical direction from $t = 0$ (bottom) to $t = 256\ \Delta t$, where $\Delta t = 0.02\ \omega_{gp\rm sw}^{-1}$. Corresponding spectra $E(r,\omega)$ and $B(r,\omega)$ are also shown on panels cg and dh; for each component of the electric and magnetic fields the Fourier transform is performed over the time domain $t = 0$ to $256\ \Delta t$, and absolute values E (and B) are calculated. With both northward and southward IMF we observe magnetosheath oscillations with a frequency about twice the local proton gyrofrequency in the simulation rest frame (note that the frequencies are Doppler shifted) as the spacecraft travels from the left to the point "MI" at the inbound magnetopause crossing. These electromagnetic oscillations are seen as time-dependent periodic variations at each spacecraft location on panels a, b, e and f, and also in the spectral analyses below. Further analysis suggests that these waves are generated by the free energy in the temperature anisotropy arising at the bow shock and locally generated as the magnetic field lines are draped around the magnetosphere. Another common feature for both flybys is the broad spectra of electromagnetic waves observed at the point of closest approach to the planet ("CA"). The spacecraft crosses Mercury's plasma belt between white marker "3" and the outbound magnetopause crossing "MO", but the broad spectra are observed only close to the planet when the belt plasma is depleted by the precipitation of ions onto Mercury's surface. Protons here are anisotropic with

$T_{p\perp} > T_{p\parallel}$ (Fig. 6dj), possibly driving the proton cyclotron and/or mirror instabilities (see Fig. 9ab and ef). Note also, however, that the physical space close to the planet has a limited size and spatial resolution as well as density and magnetic field gradients. Therefore, a more detailed analysis of the numerical results and more realistic linear predictions along with comparisons with observations are necessary.

A final feature observed in both simulations illustrated in Figure 11 pertains to the level of oscillations upstream the outbound bow shock (beyond the yellow marker "SO" on panels c-d and g-h). First, close to the bow-shock crossing, in both cases we observe electromagnetic waves as the spacecraft enters an edge of the proton foreshock. Farther upstream, when $r > 3\ R_M$, we see the spectra of numerical noise in our solar wind plasma. The noise amplitude is much smaller than that of the observed modes. There are also two qualitative differences between the two studied cases. First note the very stable current sheet with $B \approx 0$ on panel f between the white markers "2" and "3". This sheet does not change its location in time, and unmagnetized plasma here streams planetward toward the day side magnetopause (see the velocity distribution with a beam $v_x < 0$ between white markers "2" and "3" on Fig. 7d). Another difference is the broadbanded spectra observed for southward IMF (right panels) close to white marker "2", when the spacecraft enters Mercury's magnetosphere outside of the thin current sheet. The spacecraft then enters the thin current sheet just discussed where no broadbanded spectra is observed, and near white marker "3" the spacecraft re-enters the magnetospheric plasma where we again observe the broadbanded spectra of electromagnetic oscillations.

For simulation Hyb2 we determined the correlation $\langle n, B\rangle$ between the proton density n_p and the magnetic field B shown in Fig. 12. This analysis suggests that the oscillations at the inbound magnetosheath are cyclotron waves ($\langle n, B\rangle > 0$), while the magnetospheric cavity outside the thin current sheet may contain mirror waves ($\langle n, B\rangle < 0$). These results are consistent with the linear predictions of Fig. 9e and 9f. The quantities n and B in Mercury's plasma belt are weakly correlated. However, the spatial resolution may influence these results, as in the current sheet between white markers "2" and "3". Here no oscillations of B are present (as $B \approx 0$) but the density increases in order to maintain pressure balance (see Fig. 6h). This local pressure-balanced decrease of B and increase of n causes the observed (spatial) anti-correlation $\langle n, B\rangle < 0$ on Fig. 12. Oscillations in the outbound magnetosheath (between "MO" and "SO") and foreshock exhibit clear correlation ($\langle n, B\rangle > 0$), consistent with properties expected for magnetosonic waves generated in the foreshock by the upstreaming proton beam. More detailed

spectral analysis of electromagnetic oscillations are warranted and will be subject of future studies.

4. Discussion

The hybrid simulation model discussed here has some limitations. The first one is the downscaling technique. Downscaling preserves the stand-off distance of the magnetopause predicted by $R_{\rm mp} = [2B_{\rm eq}^2/(\mu_0 P_{\rm ram,sw})]^{1/6} R_M$, where $B_{\rm eq}$ is the magnetic field at the equator of the planet with radius R_M and $P_{\rm ram,sw}$ is solar wind ram pressure $n_{\rm sw0} m_p v_{\rm sw}^2$, where m_p is the proton mass ($m_p = 1$ in simulation units). The downscaling reduces the size of Mercury (and its magnetosphere) with respect to kinetic scales such as R_M/ρ_p and R_M/d_p where $\rho_p = (m_p v_{p\perp})/(eB)$ is the proton Larmor/gyro-radius and d_p is the proton inertial length. Assuming $B_{\rm sw} = 18$ nT and the (real) Mercury dipole strength to be $B_{\rm eq} = 250$ nT, the scaled down radius of Mercury used in discussed numerical experiments Hyb1 and Hyb2 was $R_M = 15.32\, d_{p\rm sw}$. The radius of Mercury is $91\, d_{p\rm sw}$ for a solar wind plasma density of 73 electrons per cm^3 and $60\, d_{p\rm sw}$ for a solar wind plasma density of 32 electrons per cm^3 (Trávníček et al., 2003), therefore, the model used in this paper represents Mercury being scaled down by a factor 4–6. Despite the downscaling, R_M used in the model is always much larger than the local proton Larmor radius. One of the consequences of the downscaling is, for example, the magnetosheath region which is also scaled down by the same factor. The magnetosheath's size limits the number of possible wavelengths for kinetic (temperature-anisotropy driven) instabilities, especially for the mirror instabilities which have long wavelengths compared to ion inertial length/gyro-radii close to instability threshold (Hellinger, 2007). The reduced flow time in the scaled down regions may also affect convective instabilities such as the Kelvin-Helmholtz one (Wright et al., 2000).

Other limitations are due to the boundary conditions. Regions close to where the bow shock hits the external system boundary in the Y and Z directions are strongly affected and the properties of the nightside magnetosheath close to the boundaries are compromised. However, most of the simulation box is not affected. The outflow boundary (at $X = 12\, R_M$) has almost no influence on the simulation results.

Finally, in our model we do not consider heavy ions such as Na^+ that originate from the planet. The densities of Na+ are expected to be very low and should not significantly alter the overall structure of the interaction between solar wind and Mercury's magnetosphere. It has been postulated that Na+ may be responsible

for the formation of the double magnetopause boundary layer observed during the first MESSENGER flyby (Slavin et al., 2008) based on Na^+ gyroradius considerations. Although this is beyond the scope pf the present study, future studies will include Na+ to examine this possibility as well as the effects of heavy ions in general on Mercury's magnetosphere.

5. Conclusions

An analysis of 3-D hybrid simulations of Mercury's magnetosphere-solar wind interaction has been presented for northward and southward IMF orientations. The overall magnetospheric features of the simulated system are similar to those in the terrestrial magnetosphere. The simulated results are in good qualitative agreement with *in situ* observations of MESSENGER spacecraft in terms of magnetospheric structure and plasma kinetic effects. The intrinsic magnetic field constitutes an obstacle to the supersonic solar wind and a typical series of thin and thick transition regions appear including bow shock, magnetosheath, magnetopause, magnetotail, magnetosphere itself, plasma belt, etc.

The oblique/quasi-parallel bow shock region is a source of backstreaming protons filling the foreshock where they generate strong wave activity (likely through the ion-ion magnetosonic instability). These large-amplitude waves are transported with the solar wind to the adjacent magnetosheath. In the quasi-perpendicular magnetosheath, waves are generated near the bow shock and locally by the proton temperature anisotropy. For the low-β plasma considered here, the dominant instability is the proton cyclotron instability, a result confirmed by the density-magnetic field $\langle n_p, B\rangle$ correlation analysis. The positions of the foreshock and the quasi-parallel and quasi-perpendicular bow shock regions are determined by the IMF orientation so their locations are naturally different in the two presented simulations. Magnetospheric plasma also exhibits a proton temperature anisotropy (loss cone) with a signature of (drift) mirror mode activity.

For both orientations magnetospheric cusps form on the day side, at higher latitudes for northward IMF compared to southward IMF, the day side magnetosphere has a smaller size for southward IMF. These differences are likely related to different locations of reconnection regions for the two orientations. Also in the case of southward IMF the night-side magnetospheric cavity in the Z direction is wider. We found strong sunward plasma flows within Mercury's magnetotail at somewhat different locations for the two IMF orientations. For southward IMF the sunward plasma flows is stronger owing to a presence a strong sunward proton beam, a signature of the reconnection process occured further downtail in the

thin current sheet (along with the formation of plasmoids). These energetic protons likely contribute to the thermal and dynamic pressure of the magnetospheric plasma widening the magnetospheric cavity in the case of southward IMF.

Both IMF configurations lead to a quasi-trapped plasma belt around the planet. Such a belt may account for the diamagnetic decreases observed on the inbound passes of both MESSENGER flybys. The quasi-trapped protons remain in the belt for several ion cyclotron periods and then either precipitate at high latitude onto Mercury's surface or hit the magnetopause and are scattered downstream exiting the magnetosphere.

For southward IMF, reconnection leads to plasmoid-like structures in the magnetotail, consistent with the second MESSENGER flyby observations in Mercury's magnetotail. On the other hand, we have not found signatures of a dayside flux transfer event. This may be a consequence of the assumed stationarity of the solar wind in our numerical model. For the northward IMF we have not found any Kelvin-Helmholtz type structure, but in an earlier simulation Hyb0 (Trávníček et al., 2009) with the IMF confined to the ecliptic plane ($B_z = 0$), signatures of Kelvin-Helmholtz instability were present. Furthermore, in both the cases the transition between the dayside magnetosheath and the magnetosphere occurs in two phases, the ion density decrease precedes the magnetopause current sheet. This is at variance with the first MESSENGER flyby where two clear current sheets (double magnetopause) are observed. This particular observation could be related to a presence of heavy planetary ions (Na^+) missing in our model. Further investigation of these problems will be subjects for future work.

Acknowledgements

The authors acknowledge the support by NASA MESSENGER grant NNX09-AD41G and NASA MESSENGER Participating Scientist grant NNX07AR62G, contract No. 300030805 from the Grant Agency of Academy of Sciences of the Czech Republic (ASCR), contract No. ME09009 of Czech Ministry of Education and PECS contract No.98068 from the European Space Agency. Simulations used for this work were performed on the Amalka supercomputing facility at Institute of Atmospheric Physics.

References

Anderson, B. J., Acuña, M. H., Korth, H., Slavin., J. A., Uno, H., Johnson, C. L., Purucker, M. E., Solomon, S. C., Raines, J. M., Zurbuchen, T. H., Gloeckler,

G., McNutt, R. L., 2009. The Magnetic Field of Mercury. Space Sci. Rev., in press.

Anderson, B. J., Acuña, M. H., Korth, H., Purucker, M. E., Johnson, C. L., Slavin, J. A., Solomon, S. C., R. L. McNutt, J., 2008. The structure of Mercury's magnetic field from MESSENGER's first flyby. Science 321, 82–85.

Baker, D. N., Odstrcil, D., Anderson, B. J., Arge, C. N., Benna, M., Gloeckler, G., Raines, J. M., Schriver, D., Slavin, J. A., Solomon, S. C., Killen, R. M., Zurbuchen, T. H., 2009. The space environment of Mercury at the time of the first MESSENGER flyby: Solar wind and IMF modeling of upstream conditions. J. Geophys. Res. 114, in press, doi:10.1029/2009JA014287.

Baker, D. N., Pulkkinen, T. I., Angelopoulos, V., Baumjohann, W., McPherron, R. L., Jun. 1996. Neutral line model of substorms: Past results and present view. J. Geophys. Res. 101, 12975–13010.

Cowley, S. W. H., 1982. Substorms and the growth phase problem. Nature 295, 365–366.

Dungey, J. W., 1961. Interplanetary magnetic field and the auroral zones. Phys. Rev. Lett. 6, 47–48.

Eraker, J. H., Simpson, J. A., 1986. Acceleration of charged particles in Mercury's magnetosphere. J. Geophys. Res. 91, 9973–9993.

Fujimoto, M., Baumjohann, W., Kabin, K., Nakamura, R., Slavin, J. A., Terada, N., Zelenyi, L., 2007. Hermean magnetosphere-solar wind interaction. Space Sci. Rev. 132, 529–550.

Gary, S. P., 1991. Electromagnetic ion/ion instabilities and their consequences in space plasmas – a review. Space Sci. Rev. 56, 373–415.

Gary, S. P., McKean, M. E., Winske, D., Anderson, B. J., Denton, R. E., Fuselier, S. A., 1994. The proton cyclotron instability and the anisotropy/β inverse correlation. J. Geophys. Res. 99, 5903–5914.

Hellinger, P., 2007. Comment on the linear mirror instability near the threshold. Phys. Plasmas 14, 082105.

Hellinger, P., Trávníček, P., 2005. Magnetosheath compression: Role of characteristic compression time, alpha particle abundances and alpha/proton relative velocity. J. Geophys. Res. 110, A04210, doi:10.1029/2004JA010687.

Hellinger, P., Trávníček, P., Kasper, J. C., Lazarus, A. J., 2006. Solar wind proton temperature anisotropy: Linear theory and WIND/SWE observations. Geophys. Res. Lett. 33, L09101, doi:10.1029/2006GL025925.

Hellinger, P., Trávníček, P. M., 2008. Oblique proton fire hose instability in the expanding solar wind: Hybrid simulations. J. Geophys. Res. 113, A10109, doi: 10.1029/2008JA013416.

Ip, W.-H., Kopp, A., 2002. MHD simulations of the solar wind interaction with Mercury. J. Geophys. Res. 107, 1348, doi:10.1029/2001JA009171.

Jackson, D. J., Beard, D. B., 1977. The magnetic field of Mercury. J. Geophys. Res. 82, 2828–2836.

Kabin, K., Heimpel, M. H., Rankin, R., Aurnou, J. M., Gómez-Pérez, N., Paral, J., Gombosi, T. I., Zurbuchen, T. H., Koehn, P. L., Dezeeuw, D. L., 2008. Global MHD modeling of Mercury's magnetosphere with applications to the MESSENGER mission and dynamo theory. Icarus 195, 1–15.

Lavraud, B., Fedorov, A., Budnik, E., Thomsen, M. F., Grigoriev, A., Cargill, P. J., Dunlop, M. W., Rème, H., Dandouras, I., , Balogh, A., 2005. High-altitude cusp flow dependence on IMF orientation: A 3-year Cluster statistical study. J. Geophys. Res. 110, A02209, doi:10.1029/2004JA010804.

Lipatov, A. S., 2002. The hybrid multiscale simulation technology: an introduction with application to astrophysical and laboratory plasmas. Springer, Berlin, New York.

Matthews, A., 1994. Current advance method and cyclic leapfrog for 2D multispecies hybrid plasma simulations. J. Comp. Phys. 112, 102–116.

Ness, N. F., Behannon, K. W., Lepping, R. P., 1975. The magnetic field of Mercury. J. Geophys. Res. 80, 2708–2716.

Ness, N. F., Behannon, K. W., Lepping, R. P., Whang, Y. C., 1976. Observations of Mercury's magnetic field. Icarus 28, 479–483.

Ness, N. F., Behannon, K. W., Lepping, R. P., Whang, Y. C., Schatten, K. H., 1974. Magnetic field observations near Mercury: Preliminary results from Mariner 10. Science 185, 151–160.

Russell, C. T., Baker, D. N., Slavin, J. A., 1988. The magnetosphere of Mercury. In: Vilas, F., Chapman, C. R., Matthews, M. S. (Eds.), Mercury. Univ. of Arizona Press, Tuscon, pp. 514–561.

Russell, C. T., McPherron, R. L., 1973. The Magnetotail and Substorms. Space Sci. Rev. 15, 205–266.

Siscoe, G., Ness, N. F., Yeates, C. M., 1975. Substorms on Mercury? J. Geophys. Res. 80, 4359–4363.

Siscoe, G. L., Christopher, L., 1975. Variations in the solar wind stand-off distance at Mercury. Geophys. Res. Lett. 2, 158–160.

Slavin, J. A., Acuña, M. H., Anderson, B. J., Baker, D. N., Benna, M., Boardsen, S. A., Gloeckler, G., Gold, R. E., Ho, G. C., Korth, H., Krimigis, S. M., Jr., R. L. M., Raines, J. M., Sarantos, M., Schriver, D., Solomon, S. C., Trávníček, P. M., Zurbuchen, T. H., 2009. MESSENGER Observations of Magnetic Reconnection in Mercury's Magnetosphere. Science 321, 606–610.

Slavin, J. A., Acuña, M. H., Anderson, B. J., Baker, D. N., Benna, M., Gloeckler, G., Gold, R. E., Ho, G. C., Killen, R. M., Korth, H., Krimigis, S. M., Jr., R. L. M., Nittler, L. R., Raines, J. M., Schriver, D., Solomon, S. C., Starr, R. D., Trávníček, P. M., Zurbuchen, T. H., 2008. Mercury's magnetosphere after MESSENGER's first flyby. Science 321, 85–89.

Slavin, J. A., Holzer, R. E., 1979. The effect of erosion on the solar wind stand-off distance at Mercury. J. Geophys. Res. 84, 2076–2082.

Slavin, J. A., Krimigis, S. M., Acuña, M. H., Anderson, B. J., Baker, D. N., Koehn, P. L., Korth, H., Livi, S., Mauk, B. H., Solomon, S. C., Zurbuchen, T. H., 2007. MESSENGER: Exploring Mercury's Magnetosphere. Space Sci. Rev. 131, 133–160.

Solomon, S. C., McNutt, R. L., Gold, R. E., Acuña, M. H., Baker, D. N., Boynton, W. V., Chapman, C. R., Cheng, A. F., Gloeckler, G., J. W. Head, III, J. W., Krimigis, S. M., McClintock, W. E., Murchie, S. L., Peale, S. J., Phillips, R. J., Robinson, M. S., Slavin, J. A., Smith, D. E., Strom, R. G., Trombka, J. I., Zuber,

M. T., 2001. The MESSENGER mission to Mercury: scientific objectives and implementation. Planet. Space Sci. 49, 1445–1465.

Solomon, S. C., McNutt, R. L., Watters, T. R., Lawrence, D. J., Feldman, W. C., Head, J. W., Krimigis, S. M., Murchie, S. L., Phillips, R. J., Slavin, J. A., Zuber, M. T., 2008. Return to Mercury: A Global Perspective on MESSENGER's First Mercury Flyby. Science 321, 59–62.

Sonnerup, B. U. O., Paschmann, G., Papamastorakis, I., Sckopke, N., Haerendel, G., Bame, S. J., Asbridge, J. R., Gosling, J. T., Russell, C. T., 1981. Evidence for magnetic field reconnection at the Earth's magnetopause. J. Geophys. Res. 86, 10049–10067.

Trávníček, P., Hellinger, P., Schriver, D., 2003. A global three dimensional hybrid simulation of the interaction between a weakly magnetized obstacle and the solar wind. In: Velli, M., Bruno, R., Malara, F. (Eds.), Solar Wind 10. Vol. 679 of AIP Conf. Proc. New York, pp. 485–488.

Trávníček, P., Hellinger, P., Schriver, D., 2007a. Structure of Mercury's magnetosphere for different pressure of the solar wind: three dimensional hybrid simulations. Geophys. Res. Lett. 34, L05104, doi:10.1029/2006GL028518.

Trávníček, P., Hellinger, P., Taylor, M. G. G. T., Escoubet, C. P., Dandouras, I., Lucek, E., 2007b. Magnetosheath plasma expansion: Hybrid simulations. Geophys. Res. Lett. 34, L15104, doi:10.1029/2007GL029728.

Trávníček, P. M., Hellinger, P., Schriver, D., Herčík, D., Slavin, J. A., Anderson, B. J., 2009. Kinetic instabilities in Mercury's magnetosphere: three-dimensional simulation results. Geophys. Res. Lett. 36, L02101, doi: 10.1029/2008GL036630.

Whang, Y. C., 1977. Magnetospheric magnetic field of Mercury. J. Geophys. Res. 82, 1024–1030.

Winske, D., 1985. Hybrid simulation codes with application to shocks and upstream waves. Space Sci. Rev. 42, 53–66.

Wright, A. N., Mills, K. J., Ruderman, M. S., Brevdo, L., 2000. The absolute and convective instability of the magnetospheric flanks. J. Geophys. Res. 105, 385–394.

Tables

Table 1: Parameters of the global hybrid simulations

	run Hyb1	run Hyb2
Spatial resolution Δx	0.4 $d_{p\mathrm{sw}}$	
Spatial resolution $\Delta y = \Delta z$	1.0 $d_{p\mathrm{sw}}$	
Spatial size of the system $L_x = N_x\,\Delta x$	237.6 $d_{p\mathrm{sw}}$	
Spatial size of the system $L_y = L_z = N_y\,\Delta y$	288 $d_{p\mathrm{sw}}$	
Mercury's radius R_M	15.32 $d_{p\mathrm{sw}}$	
Temporal resolution (simulation time step) Δt	0.02 $\omega_{gp\mathrm{sw}}^{-1}$	
Time sub-stepping for electromagnetic fields Δt_B	$\Delta t/20 = 0.001\ \omega_{gp\mathrm{sw}}^{-1}$	
Simulation box transition time	59.4 $\omega_{gp\mathrm{sw}}^{-1}$	
Duration of each simulation	120.0 $\omega_{gp\mathrm{sw}}^{-1}$	
$\beta_{p\mathrm{sw}}$	1.0	
$\beta_{e\mathrm{sw}}$	1.0	
Number of macro-particles per cell (specie 0)	80	50
Number of macro-particles per cell (specie 1)	100	100
Total number of macro-particles	$\sim 3.9\times10^9$	$\sim 2.5\times10^9$
Solar wind velocity $v_{p\mathrm{sw}}$	4.0 $v_{A\mathrm{sw}}$	
Orientation of IMF in (X, Z) plane	+ 20°	- 20°
Mercury's magnetic moment M	250 nT $R_M^3\,4\pi/\mu_0$ (no tilt)	
n_{sw}, B_{sw}, $v_{A\mathrm{sw}}$, $d_{p\mathrm{sw}}$, $\omega_{gp\mathrm{sw}}$	= 1 (in simulation units)	

Table 2: List of markers used for the orientation along the (virtual) M1 and M2 trajectories

Marker	description	color	r/R_M for M1	r/R_M for M2
"SI"	shock inbound	yellow	8.0	-
"1"		white	5.5	-
"MI"	magnetopause inbound	green	2.9	3.9
"2"		white	2.6	2.7
"3"		white	1.3	1.4
"CA"	closest approach	red	0.1	0.1
"MO"	magnetopause inbound	green	1.2	0.9
"4"		white	1.6	1.2
"SO"	shock outbound	yellow	2.1	1.6

Table 3: Fitted parameters for Eq. 2

Instability	a	b	β_0
Proton cyclotron instability	0.43	0.42	-0.0004
Mirror instability	0.77	0.76	-0.016
Parallel fire hose	-0.47	0.53	0.59
Oblique fire hose	-1.4	1.0	-0.11

Figure Captions

Figure 1. Schematic views of Mercury's magnetosphere for (left) a northward IMF highlighting the features and phenomena observed by MESSENGER during its flyby of 14 January 2008, including the planetary ion boundary layer, large flux transfer events (FTEs), flank Kelvin-Helmholtz vortices, and ultra-low-frequency plasma waves (from Slavin et al. (2008)) and for (right) a southward IMF as observed by MESSENGER on 6 October 2008. Note the strong magnetic field normal to the dayside magnetopause, the large FTEs, and the reconnection line in the near-tail region, leading to plasmoid ejection and south-north (SN) sunward-moving and anti-sunward-moving north-south(NS) traveling compression regions (TCRs), features not seen during MESSENGER's first Mercury flyby under northward IMF (from Slavin et al. (2009)).

Figure 2. Upper panels show the simulated proton density n_p in two planes: (a) the equatorial plane (X, Y) and (b) the plane of main meridian (X, Z) from simulation Hyb1 (northward IMF) at $t = 100\,\omega_{gp\mathrm{sw}}^{-1}$. The dashed white lines denote the scaled trajectory of the MESSENGER spacecraft on 14 January 2008 (referred to as M1) projected onto the two planes. Bottom panels (c) and (d) show the same information from simulation Hyb2 (southward IMF). The dashed white lines denote the scaled trajectory of the MESSENGER spacecraft on 6 October 2008 (referred to as M2) projected onto the two planes. The colored bullets demarcate various boundaries along the trajectories: yellow bullets mark inbound ("SI") and outbound ("SO") bow-shock crossings, green bullets mark inbound ("MI") and outbound ("MO") magnetopause crossings, the point of the closest approach ("CA") to Mercury's surface is marked by a red bullet, and furthermore, there are four other (white) markers referred to as "1", "2", "3", and "4" at various locations in between the boundaries. Overview of the colored markers is given in Table 2.

Figure 3. An example of a plasmoid formed in the magnetotail marked by a white arrow on panel (a) which shows simulated proton density n_p in the equatorial plane (X, Y) (southward IMF). The dashed white line displays the actual spacecraft trajectory. The colored bullets demarcate various boundaries along the trajectories, overview of the colored markers is given in Table 2. Panels (b), (c), and (d) show plasma density $n_p/n_{p\mathrm{sw}}$, Z-component of the magnetic field B_z/B_{sw},

and magnitude of the magnetic field $B/B_{\rm sw}$, respectively acquired accross the plasmoid region along the X direction.

Figure 4. Simulation results at time $t = 100\,\omega_{gp\rm sw}^{-1}$ in the two-dimensional curved sectional planes of the simulation box for (a) Hyb1 and (b) Hyb2; these planes contain the corresponding spacecraft trajectories M1 and M2, respectively, and are perpendicular to the equatorial plane (X, Y): Shown are color-scale plots of the simulated proton density n_p as a function of r and Z, where r is the distance of the corresponding position of the spacecraft from Mercury's surface. The dashed white line displays the actual spacecraft trajectory. Colored vertical bars on the panels correspond to the colored bullets used as orientation markers along the spacecraft trajectories on Fig. 2 (see also Table 2).

Figure 5. Simulation results at time $t = 100\,\omega_{gp\rm sw}^{-1}$ in the two-dimensional curved sectional planes of the simulation box for (a) Hyb1 and (b) Hyb2 simulation; these planes contain the corresponding spacecraft trajectories M1 and M2, respectively, and are perpendicular to the equatorial plane (X, Y). Shown are gray-scale plots of the magnitude of the simulated magnetic field B as a function of r and Z. The dashed black line displays the actual spacecraft trajectory. Colored vertical bars on the panels correspond to the colored bullets used as orientation markers along the spacecraft trajectories on Fig. 2 (see also Table 2).

Figure 6. Observables acquired along the M1 trajectory from simulation Hyb1 (northward IMF, left column) and those acquired along the M2 trajectory from simulation Hyb2 (southward IMF, right column). Panels a and g show the density $n_p/n_{p\rm sw}$, panels b and h show magnitude of the magnetic field $B/B_{\rm sw}$, panels c and i display the proton plasma temperature $T_p/T_{p\rm sw}$, panels d and j show the proton temperature anisotropy $T_{p\perp}/T_{p\parallel}$, panels e and k show the X-component of the plasma bulk velocity $v_{px}/v_{Ap\rm sw}$, and panels f and l displays the proton kinetic pressure $p_p/p_{p\rm sw}$. Gray dashed horizontal lines on panels d and j mark the value 1 whereas those on panels e and k mark the value 0 of the given observable. Colored vertical bars on the panels correspond to the colored bullets used as orientation markers along the spacecraft trajectory on Fig. 2 (see also Table 2).

Figure 7. Proton velocity distribution function f_p along the M1 trajectory from simulation Hyb1 with northward IMF (left panels) and along the M2 trajectory in

simulation Hyb2 with southward IMF (right panels). Panels show different cuts of f_p calculated along the corresponding spacecraft trajectory from all macro-particles within a sphere with radius $r_{\rm vdf} = 0.9 d_{p\rm sw}$: (a and d) $f_x = f_p(r, v_x, 0, 0)$; (b and e) $f_y = f_p(r, 0, v_y, 0)$; and (c and f) $f_z = f_p(r, 0, 0, v_z)$. Gray dotted lines display the corresponding mean proton velocity (a and d) $v_{px}/v_{A\rm sw}$, (b and e) $v_{py}/v_{A\rm sw}$, and (c and f) $v_{pz}/v_{A\rm sw}$. Colored vertical bars on the panels correspond to the colored bullets used as orientation markers along the spacecraft trajectory on Fig. 2 (see also Table 2).

Figure 8. Precipitation of solar wind protons onto the surface of Mercury as seen in our simulation with (a) northward IMF and with (b) southward IMF. Macro-particles were collected over a time period of $\Delta T = \omega_{gp\rm sw}^{-1}$ at $t = 100\, \omega_{gp\rm sw}^{-1}$. The longitude 0° and the latitude 0° correspond to the dayside subsolar point. Both panels show the number of protons n_p in the units of the solar wind proton density $n_{p\rm sw}$ absorbed by Mercury's surface at the given location per accumulation time $\omega_{gp\rm sw}^{-1}$ per $(c/\omega_{pp\rm sw})^2$.

Figure 9. Distance from marginal stability criteria given by Eq. 2 along spacecraft trajectory M1 in simulation Hyb1 (left panels) and along M2 in Hyb2 (right panels) for (a and e) the proton cyclotron instability, $\Gamma_{\rm pc}$, (b and f) the mirror instability, $\Gamma_{\rm mir}$, (c and g) the parallel fire hose, $\Gamma_{\rm pf}$, and (d and h) the oblique fire hose, $\Gamma_{\rm of}$. Gray dashed lines denote the value 0, and colored vertical bars on the panels correspond to the colored bullets used as orientation markers along the spacecraft trajectory on Fig. 2 (see also Table 2).

Figure 10. Magnetic field acquired along the trajectory M1 from simulation Hyb1 (northward IMF, left column) and the same observables acquired along the trajectory M2 from simulation Hyb2 (southward IMF, right column). On first six panels the three time-averaged magnetic components are shown: $\langle B_x \rangle$ (a/h, red line), $\langle B_y \rangle$ (b/i, green line), and $\langle B_z \rangle$ (c/j, blue line). The magnetic field components are given in units of $B_{\rm sw}$ and $\langle\, \rangle$ denotes time average over 256 time steps. The second six panels displays relative variations of the three magnetic components from the averaged value at time $t = 100\, \omega_{gp\rm sw}^{-1}$ $\delta B_x/\langle B \rangle = (B_x - \langle B_x \rangle)/\langle B \rangle$ (d/k, red line), $\delta B_y/\langle B \rangle = (B_y - \langle B_y \rangle)/\langle B \rangle$ (e/l, green line), and $\delta B_z/\langle B \rangle = (B_z - \langle B_z \rangle)/\langle B \rangle$ (f/m, blue line), where $\langle B \rangle = (\langle B_x \rangle^2 + \langle B_y \rangle^2 + \langle B_z \rangle^2)^{1/2}$. The last two panels (g/n) show the relative fluctuating magnetic energy $\delta B^2/\langle B \rangle^2$. The gray dashed

horizontal line on all panels marks the zero value of the magnetic field. Colored vertical bars on the panels correspond to the colored bullets used as orientation markers along the spacecraft trajectory on Fig. 2 (see also Table 2).

Figure 11. Time evolution of the absolute value of (a and e) electric $E(r,t)/(B_{\rm sw}v_{A{\rm sw}})$ and (b and f) magnetic $B(r,t)/B_{\rm sw}$ fields and the corresponding spectra (c and g) $E(r,\omega)$ and (d and h) $B(r,\omega)$ from simulation Hyb1 with northward IMF along the M1 trajectory (left) and from simulation Hyb2 with southward IMF along the M2 trajectory (right). Colored vertical bars on the panels correspond to the colored bullets used as orientation markers along the spacecraft trajectory on Fig. 2 (see also Table 2).

Figure 12. Correlation between the proton density $n_p/n_{p{\rm sw}}$ and the magnitude of the magnetic field $B/B_{\rm sw}$ along the M2 trajectory from simulation Hyb2 with southward IMF. The correlation was calculated at each measurement point over 200 nearest points and over 256 time steps. Colored vertical bars on the panels correspond to the colored bullets used as orientation markers along the spacecraft trajectory on Fig. 2 (see also Table 2).

Figures

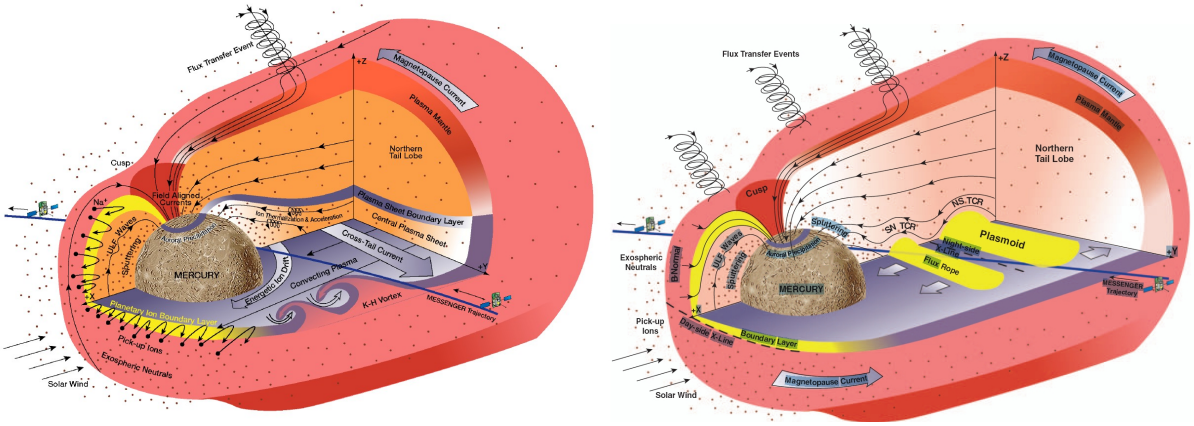

Figure 1: Schematic views of Mercury's magnetosphere for (left) a northward IMF highlighting the features and phenomena observed by MESSENGER during its flyby of 14 January 2008, including the planetary ion boundary layer, large flux transfer events (FTEs), flank Kelvin-Helmholtz vortices, and ultra-low-frequency plasma waves (from Slavin et al. (2008)) and for (right) a southward IMF as observed by MESSENGER on 6 October 2008. Note the strong magnetic field normal to the dayside magnetopause, the large FTEs, and the reconnection line in the near-tail region, leading to plasmoid ejection and south-north (SN) sunward-moving and anti-sunward-moving north-south(NS) traveling compression regions (TCRs), features not seen during MESSENGER's first Mercury flyby under northward IMF (from Slavin et al. (2009)).

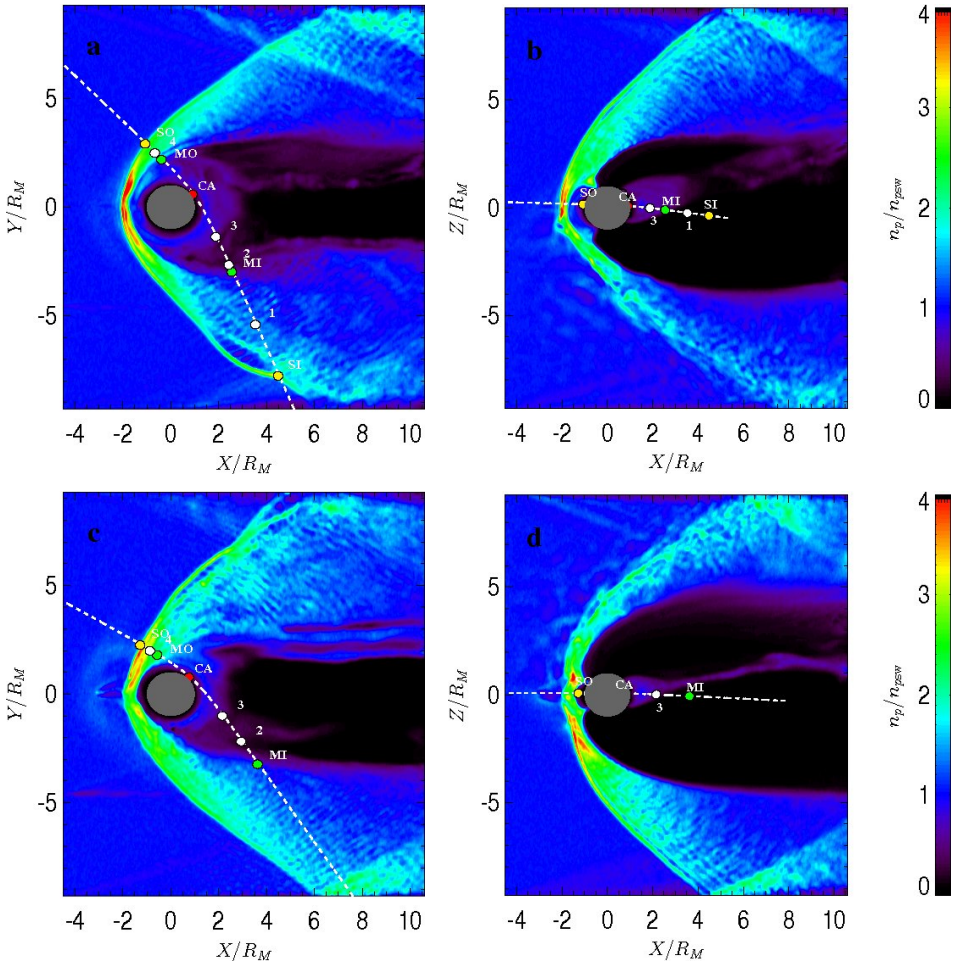

Figure 2: Upper panels show the simulated proton density n_p in two planes: (a) the equatorial plane (X, Y) and (b) the plane of main meridian (X, Z) from simulation Hyb1 (northward IMF) at $t = 100\,\omega_{gpsw}^{-1}$. The dashed white lines denote the scaled trajectory of the MESSENGER spacecraft on 14 January 2008 (referred to as M1) projected onto the two planes. Bottom panels (c) and (d) show the same information from simulation Hyb2 (southward IMF). The dashed white lines denote the scaled trajectory of the MESSENGER spacecraft on 6 October 2008 (referred to as M2) projected onto the two planes. The colored bullets demarcate various boundaries along the trajectories: yellow bullets mark inbound ("SI") and outbound ("SO") bow-shock crossings, green bullets mark inbound ("MI") and outbound ("MO") magnetopause crossings, the point of the closest approach ("CA") to Mercury's surface is marked by a red bullet, and furthermore, there are four other (white) markers referred to as "1", "2", "3", and "4" at various locations in between the boundaries. Overview of the colored markers is given in Table 2.

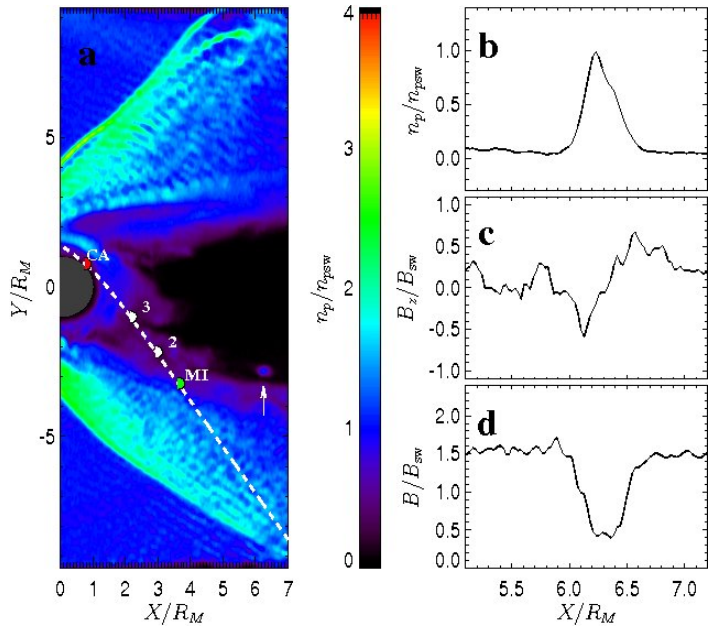

Figure 3: An example of a plasmoid formed in the magnetotail marked by a white arrow on panel (a) which shows simulated proton density n_p in the equatorial plane (X, Y) (southward IMF). The dashed white line displays the actual spacecraft trajectory. The colored bullets demarcate various boundaries along the trajectories, overview of the colored markers is given in Table 2. Panels (b), (c), and (d) show plasma density $n_p/n_{\rm psw}$, Z-component of the magnetic field $B_z/B_{\rm sw}$, and magnitude of the magnetic field $B/B_{\rm sw}$, respectively acquired accross the plasmoid region along the X direction.

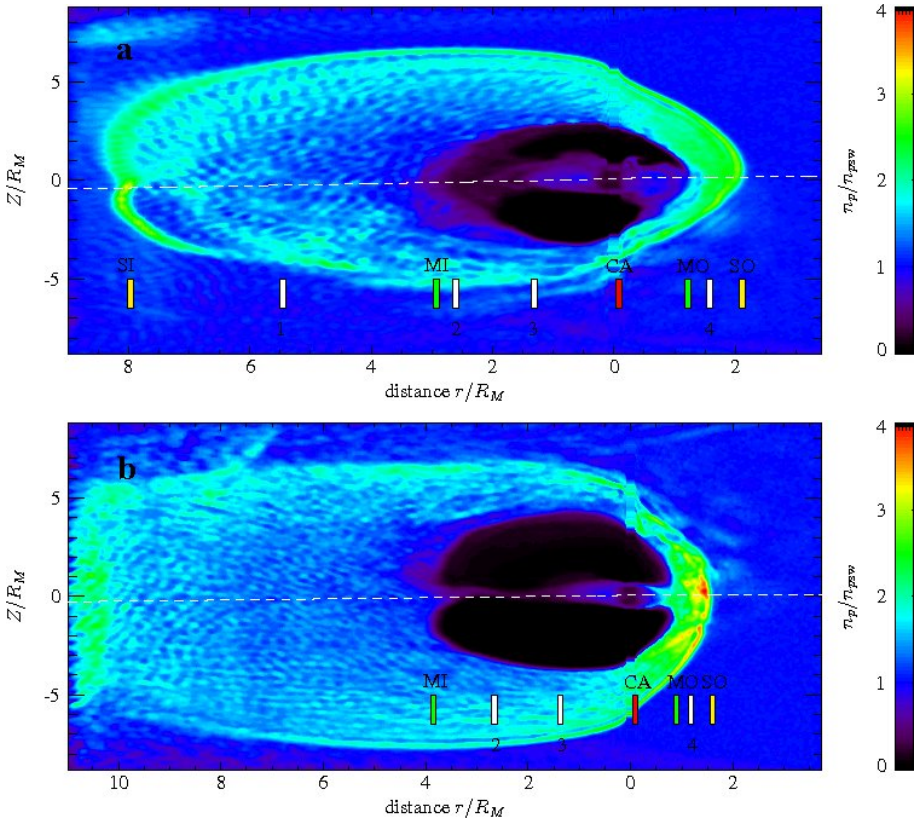

Figure 4: Simulation results at time $t = 100\,\omega_{gpsw}^{-1}$ in the two-dimensional curved sectional planes of the simulation box for (a) Hyb1 and (b) Hyb2; these planes contain the corresponding spacecraft trajectories M1 and M2, respectively, and are perpendicular to the equatorial plane (X, Y): Shown are color-scale plots of the simulated proton density n_p as a function of r and Z, where r is the distance of the corresponding position of the spacecraft from Mercury's surface. The dashed white line displays the actual spacecraft trajectory. Colored vertical bars on the panels correspond to the colored bullets used as orientation markers along the spacecraft trajectories on Fig. 2 (see also Table 2).

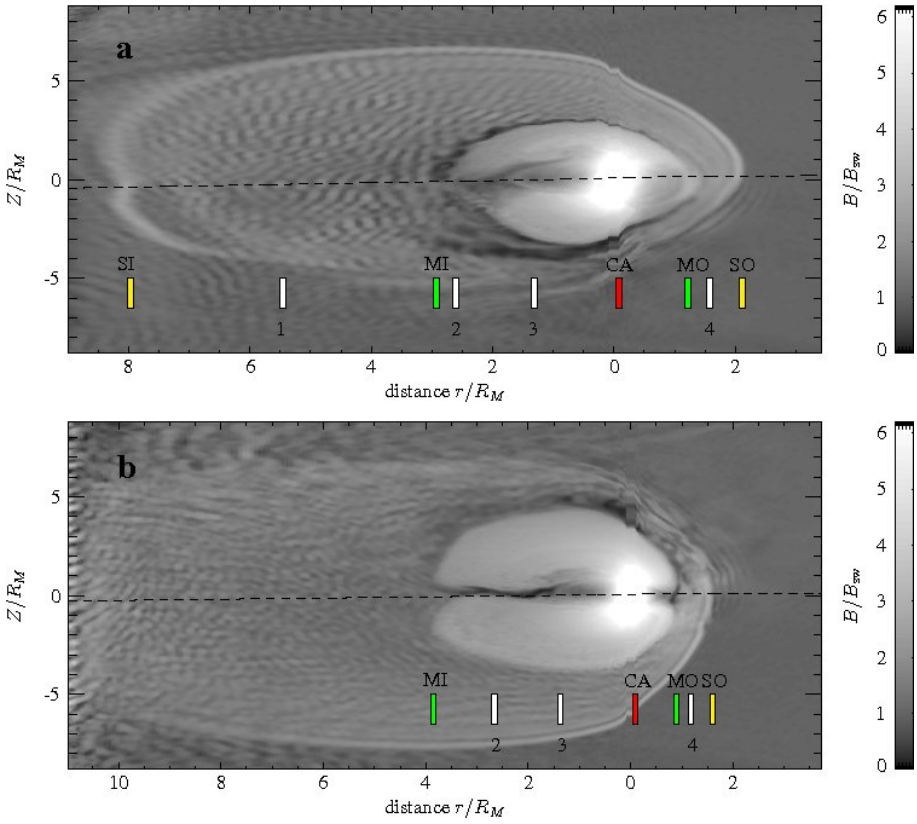

Figure 5: Simulation results at time $t = 100\,\omega_{gpsw}^{-1}$ in the two-dimensional curved sectional planes of the simulation box for (a) Hyb1 and (b) Hyb2 simulation; these planes contain the corresponding spacecraft trajectories M1 and M2, respectively, and are perpendicular to the equatorial plane (X, Y). Shown are gray-scale plots of the magnitude of the simulated magnetic field B as a function of r and Z. The dashed black line displays the actual spacecraft trajectory. Colored vertical bars on the panels correspond to the colored bullets used as orientation markers along the spacecraft trajectories on Fig. 2 (see also Table 2).

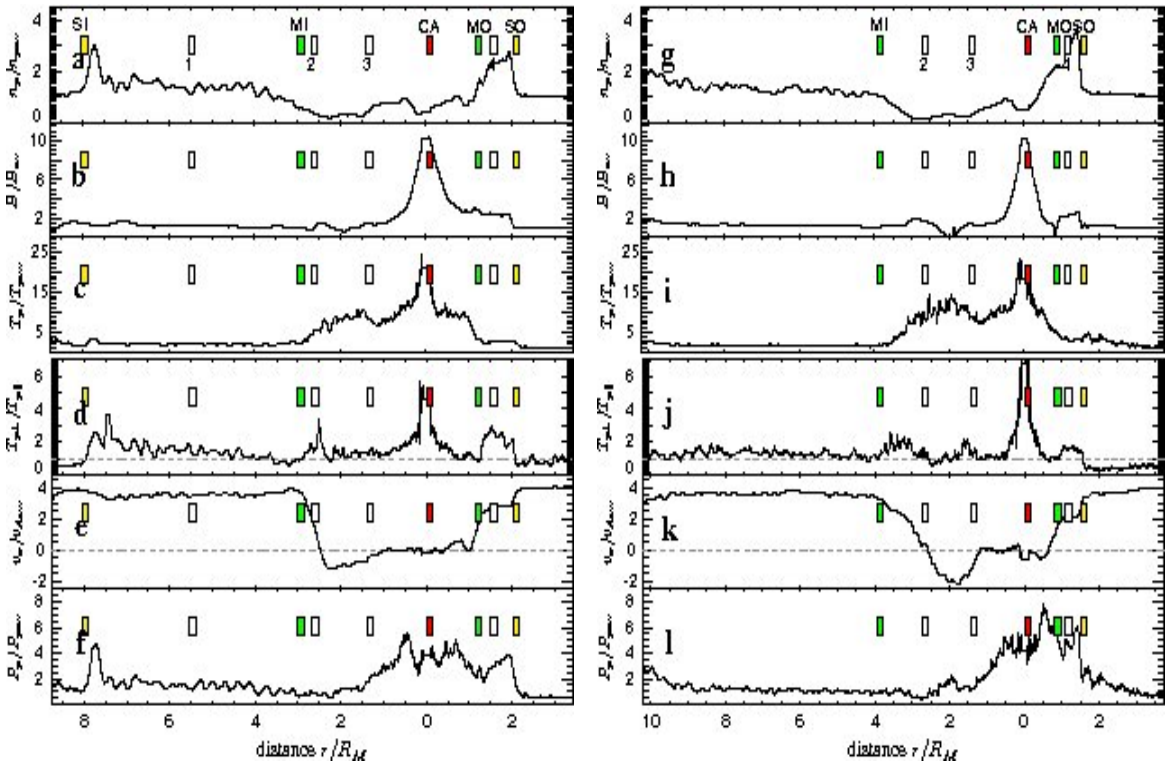

Figure 6: Observables acquired along the M1 trajectory from simulation Hyb1 (northward IMF, left column) and those acquired along the M2 trajectory from simulation Hyb2 (southward IMF, right column). Panels a and g show the density $n_p/n_{p\mathrm{sw}}$, panels b and h show magnitude of the magnetic field B/B_{sw}, panels c and i display the proton plasma temperature $T_p/T_{p\mathrm{sw}}$, panels d and j show the proton temperature anisotropy $T_{p\perp}/T_{p\parallel}$, panels e and k show the X-component of the plasma bulk velocity $v_{px}/v_{Ap\mathrm{sw}}$, and panels f and l displays the proton kinetic pressure $p_p/p_{p\mathrm{sw}}$. Gray dashed horizontal lines on panels d and j mark the value 1 whereas those on panels e and k mark the value 0 of the given observable. Colored vertical bars on the panels correspond to the colored bullets used as orientation markers along the spacecraft trajectory on Fig. 2 (see also Table 2).

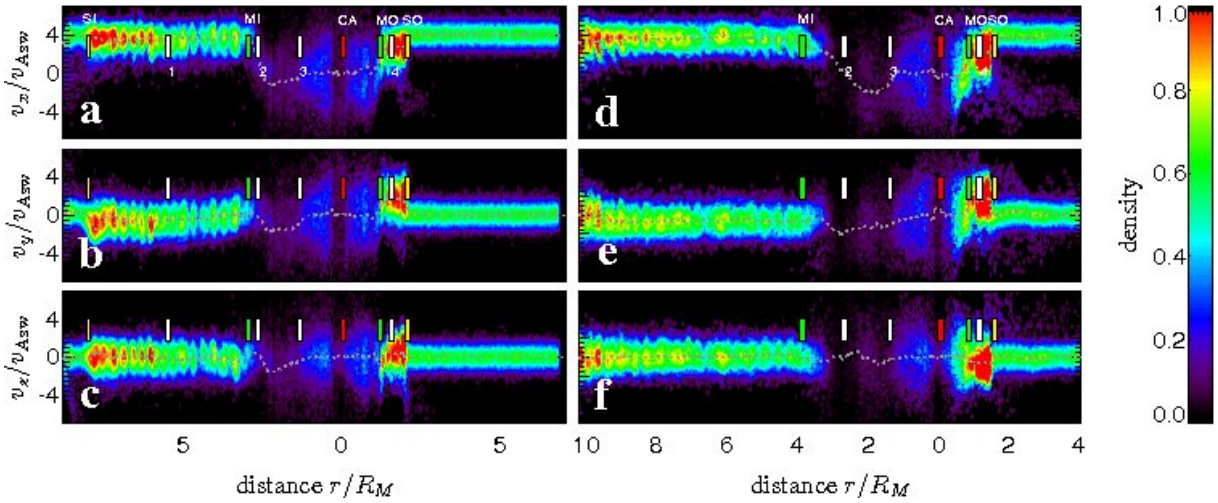

Figure 7: Proton velocity distribution function f_p along the M1 trajectory from simulation Hyb1 with northward IMF (left panels) and along the M2 trajectory in simulation Hyb2 with southward IMF (right panels). Panels show different cuts of f_p calculated along the corresponding spacecraft trajectory from all macro-particles within a sphere with radius $r_{\rm vdf} = 0.9 d_{\rm psw}$: (a and d) $f_x = f_p(r, v_x, 0, 0)$; (b and e) $f_y = f_p(r, 0, v_y, 0)$; and (c and f) $f_z = f_p(r, 0, 0, v_z)$. Gray dotted lines display the corresponding mean proton velocity (a and d) $v_{px}/v_{A\rm sw}$, (b and e) $v_{py}/v_{A\rm sw}$, and (c and f) $v_{pz}/v_{A\rm sw}$. Colored vertical bars on the panels correspond to the colored bullets used as orientation markers along the spacecraft trajectory on Fig. 2 (see also Table 2).

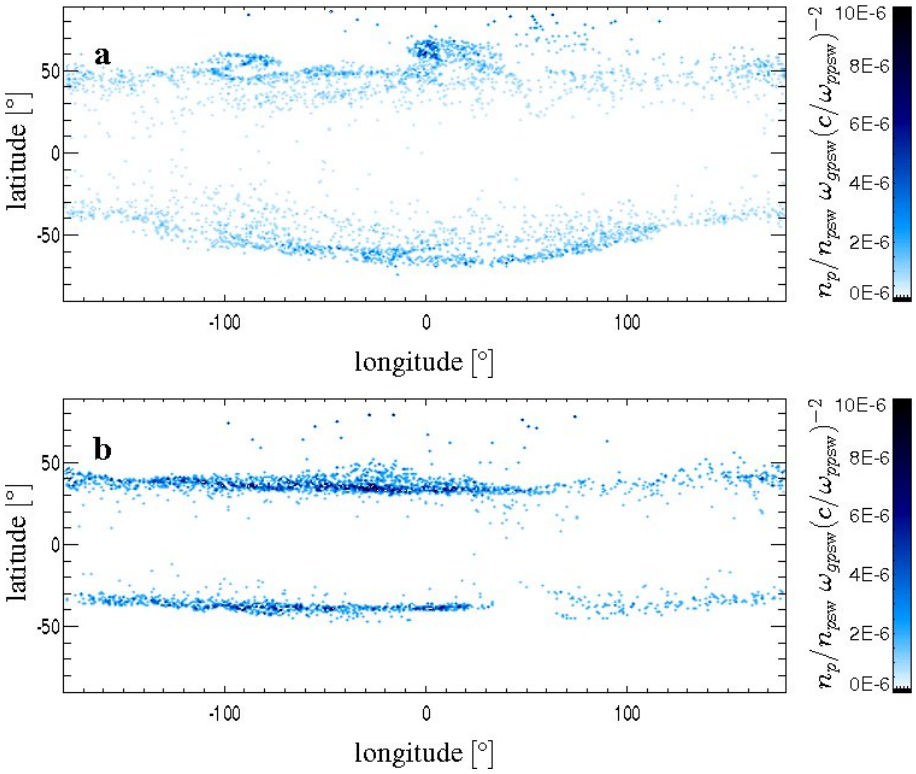

Figure 8: Precipitation of solar wind protons onto the surface of Mercury as seen in our simulation with (a) northward IMF and with (b) southward IMF. Macro-particles were collected over a time period of $\Delta T = \omega_{gp\mathrm{sw}}^{-1}$ at $t = 100\ \omega_{gp\mathrm{sw}}^{-1}$. The longitude 0° and the latitude 0° correspond to the dayside subsolar point. Both panels show the number of protons n_p in the units of the solar wind proton density $n_{p\mathrm{sw}}$ absorbed by Mercury's surface at the given location per accumulation time $\omega_{gp\mathrm{sw}}^{-1}$ per $(c/\omega_{pp\mathrm{sw}})^2$.

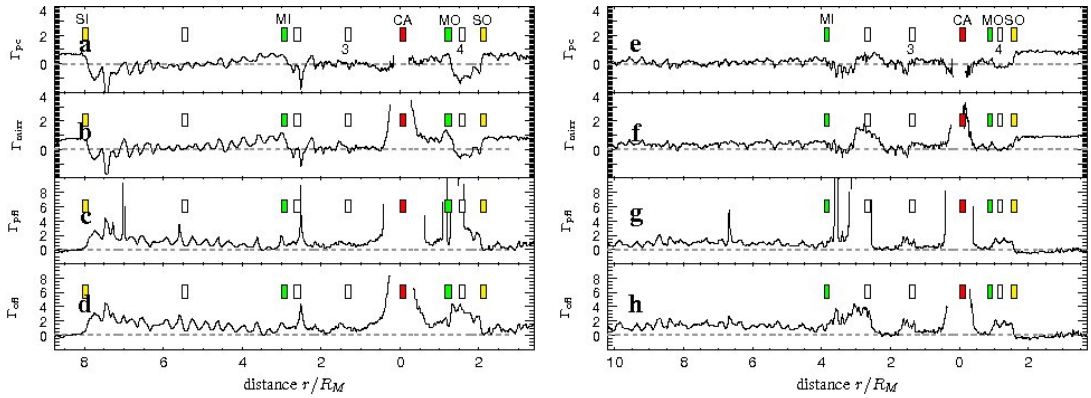

Figure 9: Distance from marginal stability criteria given by Eq. 2 along spacecraft trajectory M1 in simulation Hyb1 (left panels) and along M2 in Hyb2 (right panels) for (a and e) the proton cyclotron instability, $\Gamma_{\rm pc}$, (b and f) the mirror instability, $\Gamma_{\rm mir}$, (c and g) the parallel fire hose, $\Gamma_{\rm pf}$, and (d and h) the oblique fire hose, $\Gamma_{\rm of}$. Gray dashed lines denote the value 0, and colored vertical bars on the panels correspond to the colored bullets used as orientation markers along the spacecraft trajectory on Fig. 2 (see also Table 2).

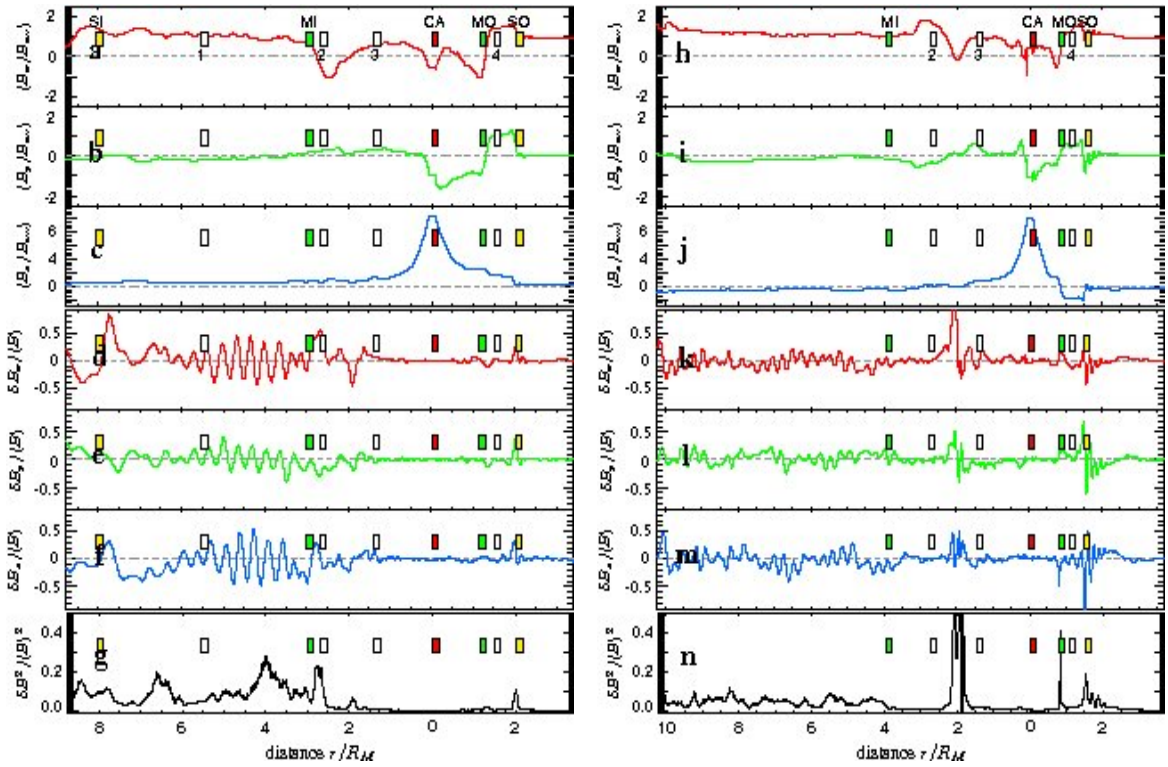

Figure 10: Magnetic field acquired along the trajectory M1 from simulation Hyb1 (northward IMF, left column) and the same observables acquired along the trajectory M2 from simulation Hyb2 (southward IMF, right column). On first six panels the three time-averaged magnetic components are shown: $\langle B_x \rangle$ (a/h, red line), $\langle B_y \rangle$ (b/i, green line), and $\langle B_z \rangle$ (c/j, blue line). The magnetic field components are given in units of $B_{\rm sw}$ and $\langle\ \rangle$ denotes time average over 256 time steps. The second six panels displays relative variations of the three magnetic components from the averaged value at time $t = 100\,\omega_{gp\rm sw}^{-1}$ $\delta B_x/\langle B \rangle = (B_x - \langle B_x \rangle)/\langle B \rangle$ (d/k, red line), $\delta B_y/\langle B \rangle = (B_y - \langle B_y \rangle)/\langle B \rangle$ (e/l, green line), and $\delta B_z/\langle B \rangle = (B_z - \langle B_z \rangle)/\langle B \rangle$ (f/m, blue line), where $\langle B \rangle = (\langle B_x \rangle^2 + \langle B_y \rangle^2 + \langle B_z \rangle^2)^{1/2}$. The last two panels (g/n) show the relative fluctuating magnetic energy $\delta B^2/\langle B \rangle^2$. The gray dashed horizontal line on all panels marks the zero value of the magnetic field. Colored vertical bars on the panels correspond to the colored bullets used as orientation markers along the spacecraft trajectory on Fig. 2 (see also Table 2).

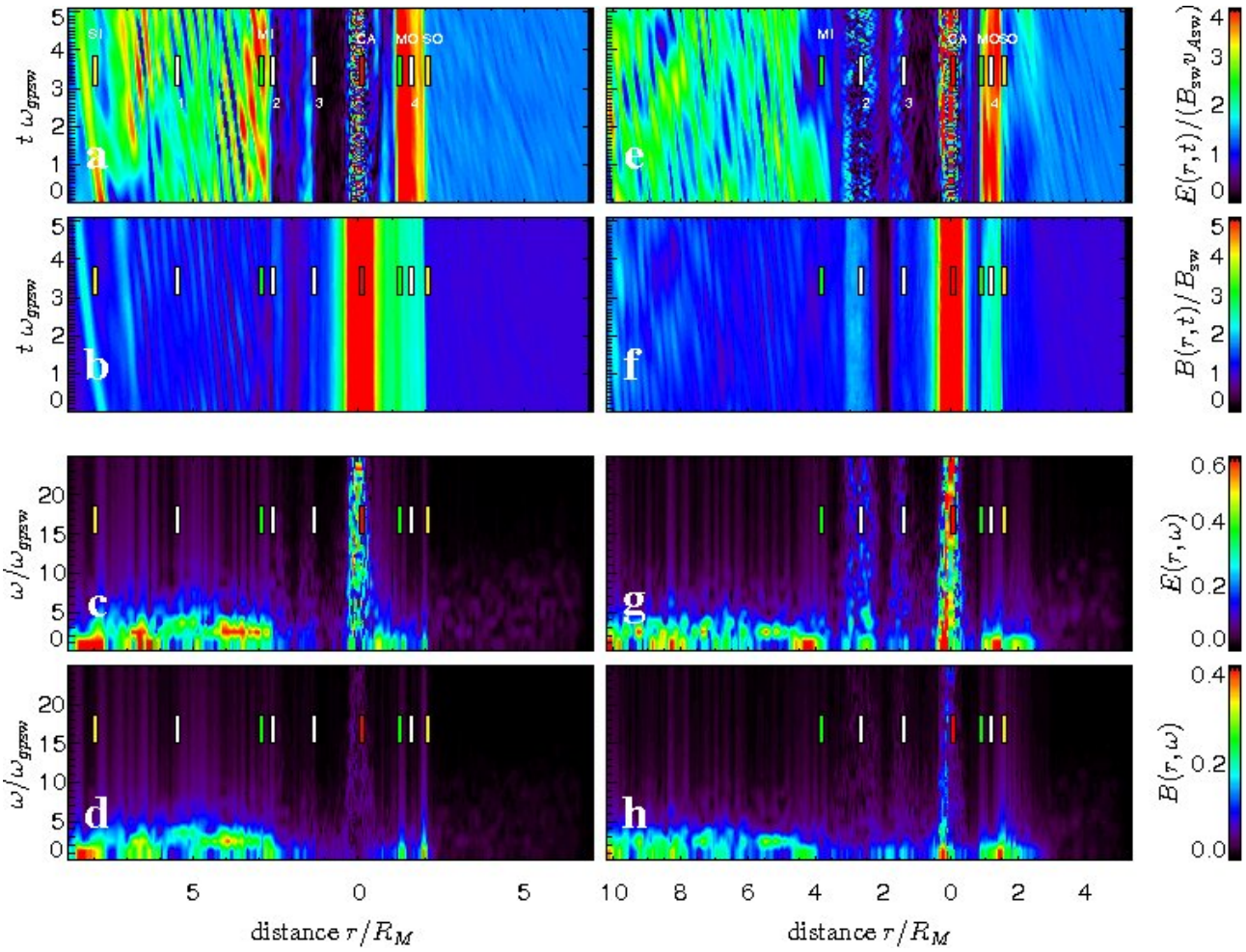

Figure 11: Time evolution of the absolute value of (a and e) electric $E(r,t)/(B_{\rm sw}v_{A\rm sw})$ and (b and f) magnetic $B(r,t)/B_{\rm sw}$ fields and the corresponding spectra (c and g) $E(r,\omega)$ and (d and h) $B(r,\omega)$ from simulation Hyb1 with northward IMF along the M1 trajectory (left) and from simulation Hyb2 with southward IMF along the M2 trajectory (right). Colored vertical bars on the panels correspond to the colored bullets used as orientation markers along the spacecraft trajectory on Fig. 2 (see also Table 2).

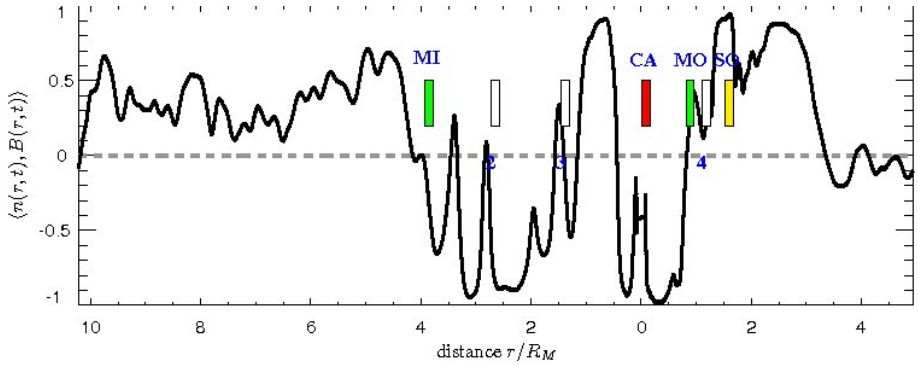

Figure 12: Correlation between the proton density $n_p/n_{\rm psw}$ and the magnitude of the magnetic field $B/B_{\rm sw}$ along the M2 trajectory from simulation Hyb2 with southward IMF. The correlation was calculated at each measurement point over 200 nearest points and over 256 time steps. Colored vertical bars on the panels correspond to the colored bullets used as orientation markers along the spacecraft trajectory on Fig. 2 (see also Table 2).